Journal of Materials Research and Technology 27 (2023) 5896–5909

Contents lists available at ScienceDirect

Journal of Materials Research and Technology

journal homepage: www.elsevier.com/locate/jmrt

Dynamic tensile deformation behavior of AISI 316L stainless steel fabricated by laser-beam directed energy deposition

N. Sommer [a,c,*], S. Lee [b,c], F. Stredak [a], C. Wolf [a], A. Suckau [a], M. Vollmer [d], S. Shao [b,c], T. Niendorf [d], N. Shamsaei [b,c], S. Böhm [a]

[a] University of Kassel, Institute of Production Technology and Logistics, Department for Cutting and Joining Manufacturing Processes, Germany
[b] Department of Mechanical Engineering, Auburn University, Auburn, AL, USA
[c] National Center for Additive Manufacturing Excellence (NCAME), Auburn University, Auburn, AL, USA
[d] University of Kassel, Institute of Materials Engineering, Metallic Materials, Germany

ARTICLE INFO

Handling editor: SN Monteiro

Keywords:
Additive manufacturing
Directed energy deposition
316L stainless steel
Dynamic tensile deformation
Recrystallization heat-treatment
Twinning

ABSTRACT

The dynamic deformation behavior of metallic materials is the key to crash-safe design in many applications, e.g., in the automotive sector. However, in the field of additive manufacturing, dynamic deformation properties have only been scarcely studied. Based on the intrinsic interrelationships of process parameters, post-process heat treatments and the resulting microstructure, the present study seeks to provide a holistic overview of the dynamic tensile deformation properties of AISI 316L stainless steel, fabricated by laser-beam directed energy deposition. Utilizing *in situ* digital image correlation, the local deformation behavior at varying strain rates from 100 s^{-1} to 1000 s^{-1} was unveiled. In combination with pre- and post-mortem microstructure analysis using electron backscatter diffraction and scanning transmission electron microscopy, the microstructural effects on the active deformation mechanisms were studied. The results show that twinning contributes to the overall deformation in the heat-treated condition owing to the weaker crystallographic texture. On the contrary, twinning is less prominent in the non-heat-treated condition due to its pronounced <001> texture. As a result of the differences in terms of active deformation mechanisms, superior fracture elongations are observed in heat-treated condition, which are rationalized by delayed necking due to a more homogeneous strain distribution along the gauge section. Independently from the sample condition, fractography analysis revealed a ductile mode of failure being characterized by equiaxed dimples on the fracture surfaces. Consequently, it can be concluded that AISI 316L stainless steel is excellently suited for dynamic tensile loading, although heat-treatment-depended differences have to be taken into account.

1. Introduction

Additive manufacturing (AM) enables the fabrication of parts with unprecedented geometrical freedom and complexity [1]. Within the class of metallic materials, laser-beam powder-bed fusion (PBF-LB) and directed energy deposition (DED-LB) are among the most prominent fabrication techniques [2]. In contrast to PBF-processes, DED-processes are characterized by the direct feed of wire- or powder-material to the process zone [3]. Moreover, the use of two or more powder-hoppers during DED-LB facilitates the *in situ* fabrication of compositionally-graded parts [4,5], which is found to be particularly suitable for high-throughput alloy development [6]. On top of that, the maximum build envelope of the parts in PBF-processes is limited to the size of the chamber, whereas parts for DED processes are not as much restricted in size [7], making it attractive for large-scale components. Contrary to PBF-processes, state-of-the-art DED-LB machinery may also be supplemented with subtractive manufacturing methods, i.e., milling, in the same building chamber and, thus, enable a swift and productive post-processing of the respective component to high geometrical accuracy or smooth surface finish [8]. Regardless of the AM-process employed, it has been reported that the inherent solidification and cooling characteristics may lead to epitaxial grain growth and/or pronounced texture upon application of distinctive process parameters [9–11], potentially causing anisotropic mechanical properties [12].

* Corresponding author. University of Kassel, Institute of Production Technology and Logistics, Department for Cutting and Joining Manufacturing Processes, Germany.
E-mail address: n.sommer@uni-kassel.de (N. Sommer).

https://doi.org/10.1016/j.jmrt.2023.10.251
Received 4 August 2023; Received in revised form 5 October 2023; Accepted 24 October 2023
Available online 7 November 2023

Therefore, it is of great importance to correlate the microstructural features with the obtained mechanical properties [13,14] and study the effects of post-AM heat-treatments on the characteristics described beforehand, as heat-treatments have proved to be effective to tailor the microstructure after AM-processing [15].

Many publications detail such interrelationships for quasi-static or cyclic loading/fatigue [16–18] and fatigue crack growth [19]. On the contrary, only very limited research has been conducted on the properties of additively manufactured (AM) materials at very high strain rates, which is the key for crash-safe design in various industries [20], e.g., automotive or aerospace, as recent reviews underline [21]. In the field of lightweight aluminum alloys, research has been focused on dynamic properties of AlSi10Mg fabricated by PBF-LB, either under compression [22–25] or tension [26], using the Split Hopkinson Pressure Bar (SHPB) and Split Hopkinson Tension Bar (SHTB), respectively. For example, studies using a SHTB on Scandium-alloyed grade AA5028 by Jakkula et al. [27] pinpoint a superior failure strain upon increasing strain rates.

Another lightweight alloy frequently used in AM, Ti6Al4V, was studied under dynamic tensile loading with intentionally induced, spherical defects of varying diameter by Fadida et al. [28] using a SHTB setup at a nominal strain rate of 1000 s^{-1}. Results indicated the existence of a critical pore diameter below which necking and fracture were not induced at the pore under dynamic loading, which was rationalized by the propagation of stress waves in the tested sample leading to a pile-up of plastic strains within the sample [28]. Within the class of Ni-based alloys, the dynamic response of Inconel 625 fabricated by PBF-LB was studied by Du et al. [29] using SHPB- and SHTB-setups. It was reported that the dynamic yield strength of the alloy increased noticeably with increasing strain rate, although specimens under tensile loading not exhibited any necking [29].

Stainless steels, which are frequently used for AM due to their widespread application in numerous industries on the basis of a well-balanced portfolio of ductility, strength and corrosion resistance, have only been scarcely studied in literature with regard to their dynamic properties [30–34]. First reports on the spallation response of AISI 316L stainless steel (SS), fabricated by powder-fed DED-LB (DED-LB/M) were published by Gray et al. [30]. A comparison between the non-heat-treated and recrystallized condition, enabled by a post fabrication heat treatment, of AM samples as well as a wrought plate was provided through quasi-static compression experiments. These tests revealed a substantially increased yield strength of the non-heat-treated condition in contrast to both recrystallized and wrought samples, which was attributed to the fine dendritic substructure of the non-heat-treated condition. However, during spallation experiments, failure of the specimens loaded parallel to build direction (BD) was found to predominantly occur along the melt pool boundaries of the non-heat-treated specimens contrary to the other conditions. Based on this work, Gray et al. [31] further investigated the dynamic compression behavior of similar AISI 316L SS sample conditions using a SHPB-setup at nominal strain rates of 1200 s^{-1}. It was found that the three aforementioned sample conditions exhibited identical work hardening behaviors, although the non-heat-treated sample showed a substantially increased yield strength and flow stress. This observation was ascribed to a fine inter-dendritic matrix contributing to strengthening according to the Hall-Petch relationship [31].

Recently, Chen et al. [32] conducted dynamic compression tests using a SHPB-setup with strain rates ranging from 690 s^{-1} to 4320 s^{-1} on AISI 316L SS fabricated by the so-called cold metal transfer, a wire-fed arc welding AM process, as well as on wrought specimens. Similar to previous reports, the yield strength of the non-heat-treated condition was significantly higher than in the wrought plate. While the microstructure was characterized by columnar grain growth in BD, Chen et al. [32] did not notice a mechanical anisotropy during dynamic compression testing. These tests further revealed no influence of strain rate on the yield strength or flow stress during compressive loading. A *post-mortem* microstructure analysis provided information on the prevailing deformation mechanism including twinning. The twins seen varied in thickness and density in relation to the employed strain rate [32].

Table 1
Chemical composition of the employed AISI 316L SS powder as provided by the material supplier, in wt.-%. Data were determined using optical emission spectroscopy and hot gas extraction (carbon).

C	Mn	P	S	Cr	Mo	Ni	Fe
0.03	0.5	0.015	0.011	16.5	2.1	13.0	bal.

In addition to the aforementioned studies on AISI 316L SS, Nishida et al. [33] as well as Song et al. [34] investigated the dynamic behavior of DED-LB/M AISI 304L SS in non-heat-treated and wrought conditions under compression (SHPB) and tension (SHTB), respectively. While AISI 304L SS was characterized by a higher yield strength and flow stress in the non-heat-treated condition in both studies [33,34], the latter one also revealed a substantial reduction of fracture elongation in the non-heat-treated condition under tensile loading [34]. In summary, the literature underlined the importance of understanding the process-microstructure-property interrelationships of AM components under dynamic loading. Yet, the presented state-of-the-art lacks an investigation on the properties of AISI 316L SS under dynamic tensile loading and, moreover, its local deformation behavior.

In consideration of the differences between compression and tension in the AISI 304L SS described above, this work thus focuses on the dynamic deformation properties of AISI 316L SS, fabricated by DED-LB/M, under tensile loading with strain rates of up to 1000 s^{-1}. The dynamic tensile tests are coupled with *in situ* digital image correlation (DIC) to shed light on the strain distribution and inherent deformation mechanisms during high strain rate loading, which — to the best of the authors knowledge — have not been documented in literature before. Prior to the dynamic tensile tests, the robustness of DED-LB/M processing is characterized by X-ray computed tomography (CT) while the microstructural evolution is analyzed using electron backscatter-diffraction (EBSD) in both *pre-* and *post-mortem* conditions. In conjunction with fractography analysis, this study provides a holistic overview of the interrelationships between microstructure, defects and dynamic tensile properties, for which pathways toward crash-safe AM-components are paved.

2. Experimental

2.1. Materials and process setup

AISI 316L SS powder with a nominal powder particle size range of 50–150 μm and chemical composition given in Table 1 was used as feedstock material. As substrate materials, AISI 304 SS sheets with nominal dimensions of 50 × 50 × 10 mm^3 were employed.

Specimen fabrication was conducted using a DED-LB/M system consisting of a six-axis robot (Reis RV 30–26, Reis GmbH & Co. KG, Obernburg, Germany) and a 2 kW fiber-laser (IPG YLS-2000-S2, IPG Photonics GmbH, Burbach, Germany) with a top-hat intensity profile. The beam was guided to the focusing optics using an optical fiber with a diameter of 400 μm. The use of focusing and collimating lenses with focal distances of 300 mm and 100 mm, respectively, yielded an approximate beam diameter of 1.2 mm on the workpiece surface in the laser beam focal plane. The powder was fed to the process zone using two-disk powder feeder (GTV PF2/2, GTV Verschleißschutz GmbH, Luckenbach, Germany) and a three-jet, coaxial nozzle (Fraunhofer ILT, Aachen, Germany) with a standoff distance of 12 mm. To prevent oxidation of the build during fabrication, Argon shielding and carrier gas (purity >99.996 %) was fed to the process zone with flow rates of 20 L/min and 5 L/min, respectively. Through the established setup, rectangular samples with approximate dimensions of 50 × 20 × 70 mm^3

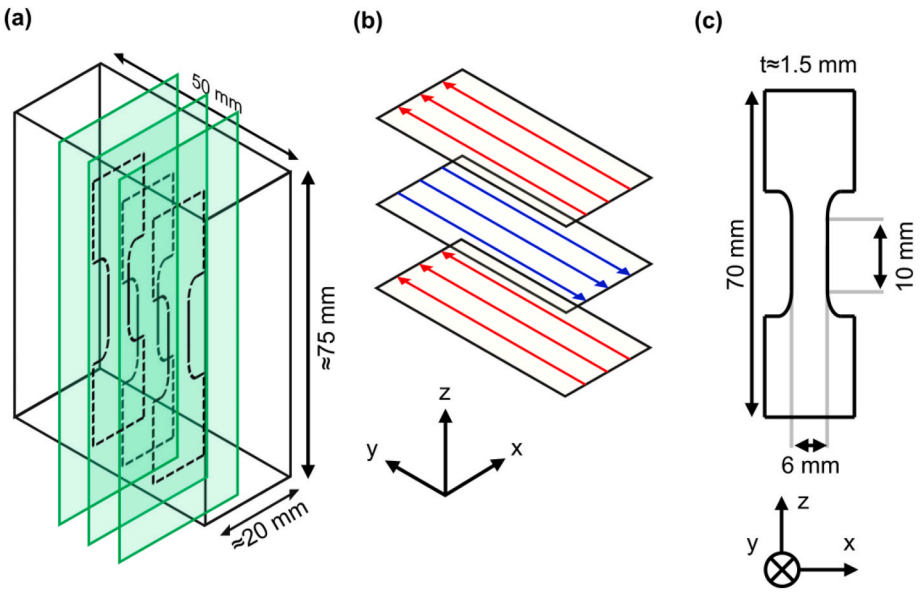

Fig. 1. Schematic illustrations introducing (a) the sample geometry with indications of approximate size and location of tensile testing specimens, (b) visualization of the employed quasi bi-directional scanning strategy, colored arrows indicate the robot trajectory within each deposited layer, and (c) the depiction of the dimensions of the tensile testing geometry.

(length × width × height, see Fig. 1 (a) for schematic drawing) were fabricated using a laser power of 1000 W, a traverse speed of 600 mm/min and powder mass flow of 14.9 g/min. Throughout sample fabrication, a quasi-bi-directional scanning strategy was employed, which alters the robot trajectory after every deposited layer, as is schematically illustrated in Fig. 1 (b).

The hatch distance was kept constant at 1 mm while the layer spacing (step size in z-direction) was maintained at 0.85 mm throughout the build, thus establishing a volumetric energy density of 117.65 J/mm^3. The process parameters were elaborated on the basis of multi-track studies conducted previous to the investigation herein. A total of two sample batches were fabricated. While batch A was investigated in the non-heat-treated condition, batch B underwent a recrystallization anneal at 1060 °C for a duration of 2 h followed by water quenching. For the sake of readability, the abbreviation NHT for non-heat-treated and HT for heat-treated shall be used in the text and figures throughout the remainder of this article. Subsequently, the surface of both samples was milled and tensile testing specimens with a nominal thickness of 1.5 mm and parallel gauge length of 10 mm were extracted parallel to the xz-plane as is visualized in Fig. 1 (c). Please note that this reference coordinate system will be used throughout the present study and that the z-axis consequently marks the BD.

2.2. Sample characterization

First, the robustness of DED-LB/M processing of each additively manufactured batch was assessed using a representative tensile specimen extracted from each batch employing micro-computer tomography (Zeiss Xradia Versa 520, Carl Zeiss AG, Oberkochen, Germany) with an effective voxel size of 21.25 μm. Furthermore, etched cross-sections were investigated using optical light microscopy (Leica DM2600, Leica Microsystems GmbH, Wetzlar, Germany). The cross-sections were mechanically ground using SiC-paper (grit size 800 to 4000), polished using colloidal silica (grit size 0.1 μm) and subsequently underwent an electrolytic etching routine (ATM Kristall 680, ATM Qness GmbH, Mammelzen, Germany) at 3 V for 5 min in a solution on basis of perchloric acid ($\rho = 1.458$ g/cm^3) and ethanol ($\rho = 0.85$ g/cm^3). Porosity quantifications were obtained via image processing using ImageJ (version 1.54 d) through an automated binarization routine. The microscopy images were captured at a resolution of 2048 px x 1536 px at 50× magnification, thus yielding an analysis precision of approximately 0.86 px/μm. Following binarization, the porosity was evaluated using the proprietary feature "Analyze Particles" of ImageJ. The boundary conditions for size and circularity of the porosity detection set ranged from 0 μm^2 to 200 μm^2 and 0.00 to 1.00, respectively.

Microstructure investigations were performed centrically along the gauge length of the tensile testing specimens. In order to reveal the microstructural evolution, samples were mounted in hot-curing epoxy resin, mechanically ground using SiC-paper (grit size 320 to 4000) and polished using SiO_2 solution (grit size 0.05 μm) with a ChemoMet polishing cloth. Subsequently, the samples were inspected using electron backscatter diffraction (EBSD, Oxford Symmetry, Oxford Instruments plc, Abingdon, United Kingdom). A scanning electron microscope equipped with a Gallium-based focused iron beam (FIB-SEM, Zeiss Crossbeam 550, Carl Zeiss Microscopy GmbH, Oberkochen, Germany) was used for this purpose. EBSD analysis was conducted at 100× magnification, electron acceleration voltage of 20 kV and a step size of 0.8 μm.

2.3. Dynamic tensile testing

Dynamic tensile tests were conducted using a high-speed tensile testing machine (HTM 8020, Zwick Roell GmbH & Co. KG, Ulm, Germany) and a load cell with a maximum capacity of 80 kN. The tests were carried out at ambient temperature with nominal strain rates of 100 s^{-1}, 500 s^{-1} and 1000 s^{-1}. Using this system, the plastic deformation of the samples is caused by the transformation of kinetic energy induced by the accelerated piston of the tensile testing machine. Eventually, this dynamic acceleration causes vibration of the entire test rig, particularly at high strain rates. As has been reported in a previous publication of some of the present authors [35], this leads to a wavy character of the obtained stress-strain curves and is not related to the intrinsic material behavior itself. To account for this waviness of the respective stress-strain curves, the moving mean (MM) with an interval of 15 data points was calculated from the datasets and plotted with the corresponding data points.

In order to obtain information on the strain evolution of the tensile specimens during dynamic testing, the test rig is equipped with a digital image correlation (DIC) setup. To allow for robust DIC, all tensile testing specimens were sprayed with a bicolor surface pattern prior to testing in

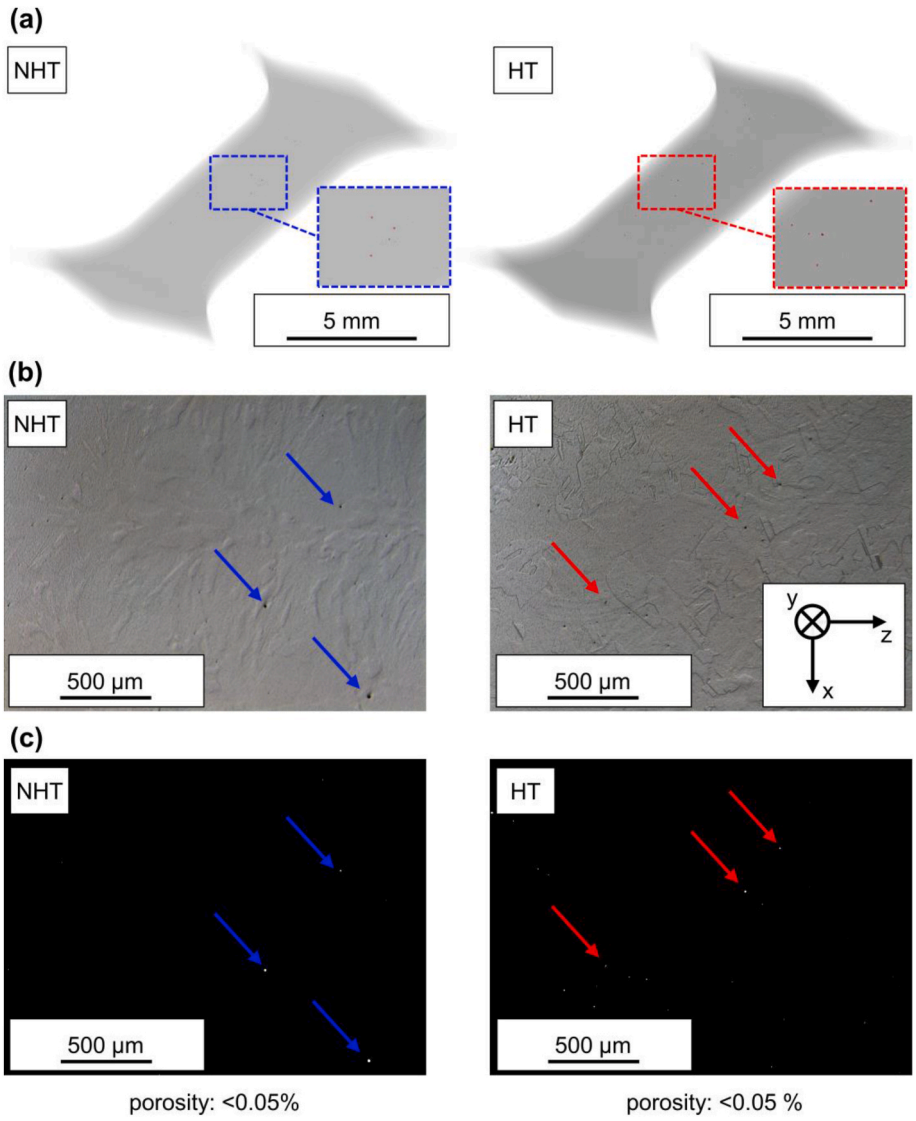

Fig. 2. Assessment of robustness of DED-LB/M processing through (a) X-ray computed tomography of representative tensile testing specimens in isometric view and (b) etched cross-sections obtained using optical microscopy. Binary images were obtained based on calculated levels of porosity and are depicted in (c). The color-coded arrows indicate pore formation, which appears as white on black background.

order to facilitate enhanced contrast. The DIC system consists of a stereographic array of two high-speed cameras (FASTCAM SA-X2, Photron Europe ltd., High Wycombe, United Kingdom) operated at a framerate of 100,000 frames per second during the experiments. The obtained strain data were processed and analyzed using commercially available software (VIC-3D, Correlated Solutions Inc., Irmo, SC, USA). It shall be noted that the derived global strain data consequently represent the Lagrangian strain in build direction (ε_{zz}) throughout the present study. The obtained strain data were fitted to the resulting load and displacement data, obtained at a frequency of 1 MHz, through alignment of the final image frame before rupture and the drop of force as detected by the load cell of the tensile testing rig.

2.4. Post-mortem characterization

Following tensile testing, the fracture surfaces of the specimens were inspected by a field-emission SEM (FE-SEM, Zeiss REM Ultra Plus, Carl Zeiss Microscopy GmbH, Oberkochen, Germany) operated at an acceleration voltage of 15 kV and an aperture size of 30 µm. Additionally, overviews of the fractured tensile testing specimens were obtained by means of optical microscopy (Leica Z16, Leica Microsystems GmbH, Wetzlar, Germany). In order to allow for microstructural characterization of the deformed microstructure in *post-mortem* condition and in immediate vicinity of the failure region, the fractured specimens underwent EBSD preparation on the xz-plane through mounting in cold-curing epoxy resin and subsequent grinding with SiC-paper (grit size 800 to 2500). Afterwards, the samples were polished with diamond solution (grit size 0.05 µm) before the cold-curing epoxy resin was mechanically removed. Samples were then inspected using EBSD (Bruker e−flash) in the aforementioned FE-SEM operated at an acceleration voltage of 20 kV and an aperture size of 120 µm. Images were acquired at 200× magnification and a step size of 0.5 µm. Furthermore, an in-depth analysis of the deformed microstructure was conducted using *in situ* sample preparation in the FIB-SEM. Lamellae trenches were milled in a three-step approach using a Ga^+ acceleration voltage of 30 kV and currents of 7 nA, 1.5 nA and 300 pA, respectively. Thinning was performed following lift-out with an acceleration voltage of 30 kV, at Ga^+ currents of 50 pA, 20 pA and 10 pA. The lamellae were inspected by means of scanning transmission electron microscopy (STEM) using the aforementioned FIB-SEM operating at an acceleration voltage of 30 kV and an electron beam current of 100 pA.

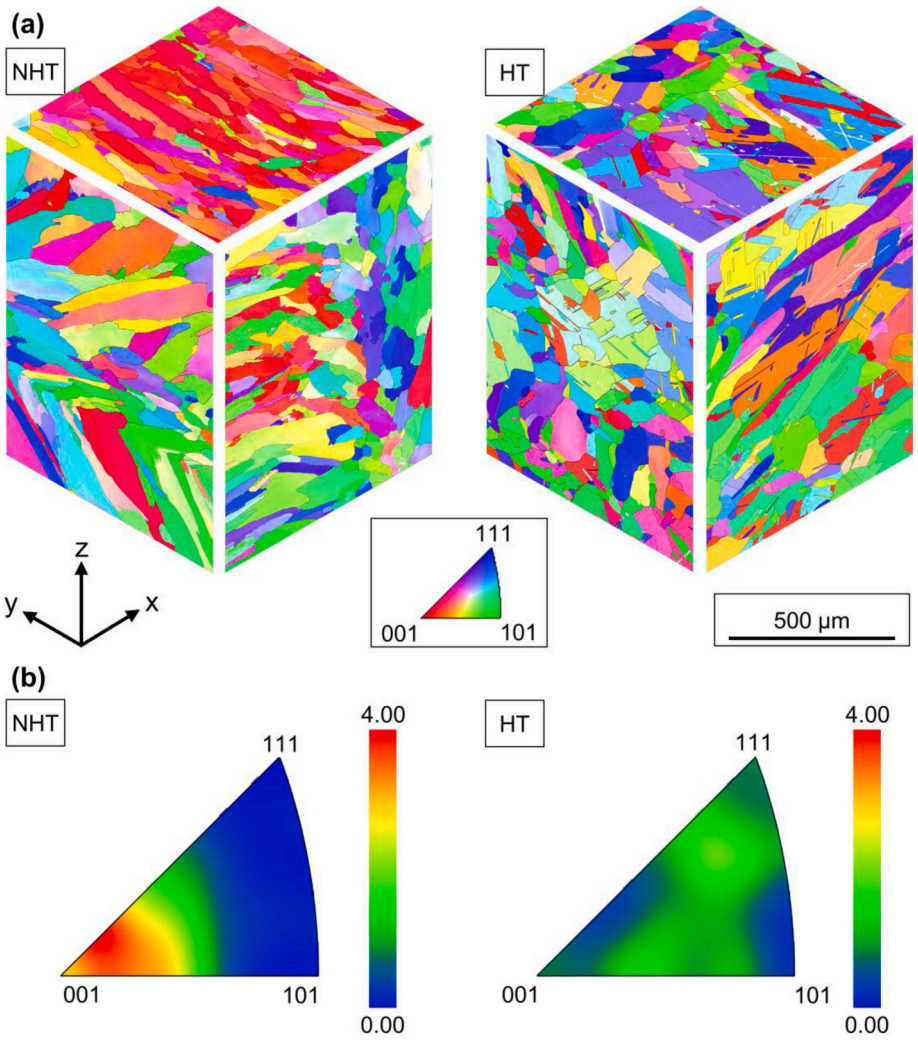

Fig. 3. Microstructural appearance of the DED-LB/M processed samples: (a) isometric views of the inverse pole figure orientation mappings along sample planes as indicated by the coordinate system. Grain orientations are plotted with respect to the z-axis (BD); (b) texture analysis (inverse pole figures) for the xy-plane calculated from EBSD data, where orientation distributions are plotted for the z-axis only.

3. Results and discussion

3.1. Microstructural evolution

The assessment of robustness of processing via micro-CT in Fig. 2 (a) reveals the formation of some porosity, highlighted in red on the magnified inset images (note that the image borders are color-coded in blue for NHT and red for HT). Focus of the present work only was on the assessment of porosity and lack of fusion defects with sizes above 25 µm as smaller defects were not considered critical for the relatively ductile material, i.e., AISI 316L [36,37].

Furthermore, it is to be perceived that the size and density of the identified porosity is independent from the specimen condition, i.e., NHT or HT. In addition, the porosity features circular shapes throughout, thus indicating the formation of pores during the fabrication process or stemming from hollow powder particles or an entrapment of shielding gas within the melt, which can be distinguished from the irregularly-shaped defects known as lack of fusion [38]. The etched micrographs in Fig. 2 (b) confirm this observation and further illustrate that the size of the identified pores is well below 100 µm. Moreover, binary images in Fig. 2 (c) allow for porosity quantification (given as area fraction) in each specimen condition and demonstrate similar levels of porosity with values below 0.05 % for both NHT and HT conditions. Based on the results it can be concluded that the employed process parameters yield nearly full-dense parts.

The approximate laser intensity I_L used throughout the experiments, given by the relationship $I_L = P_L/A_L$, where P_L denotes the laser power and A_L the area of the laser beam in its focal plane [39], can be calculated as approximately 8.84×10^4 W/cm^2. Thus, the applied intensity level is far below the threshold of 1×10^6 W/cm^2 required for deep-penetration welding in iron-based alloys [40]. Consequently, it can be deduced that the observed, spherical pores in the tensile testing specimens are unlikely keyhole pores [38], but rather entrapment of either shielding or carrier gas in the melt or introduced by hollow powder particles. Previous studies attributed the observation of gas porosity in samples fabricated by DED-LB/M to a distinctive combination of shielding gas flow and powder mass flow, while the overall increase of shielding gas facilitated greater gas porosity [41]. As a result of this observation, a reduction of the employed shielding gas flow to a value below 20 L/min, being applied in the present study, may further decrease the level of gas porosity. Nevertheless, the identified degrees of gas porosity within both representative specimens are well below the optimized parameter set in Ref. [41].

The microstructure of the two sample batches is characterized by significant differences, as is visualized in Fig. 3 (a).

The inverse pole figure orientation mapping (IPFM) acquired for the yz-plane of NHT sample, i.e., along the laser trajectory in each respective layer, highlights the growth of columnar grains with an elongated shape.

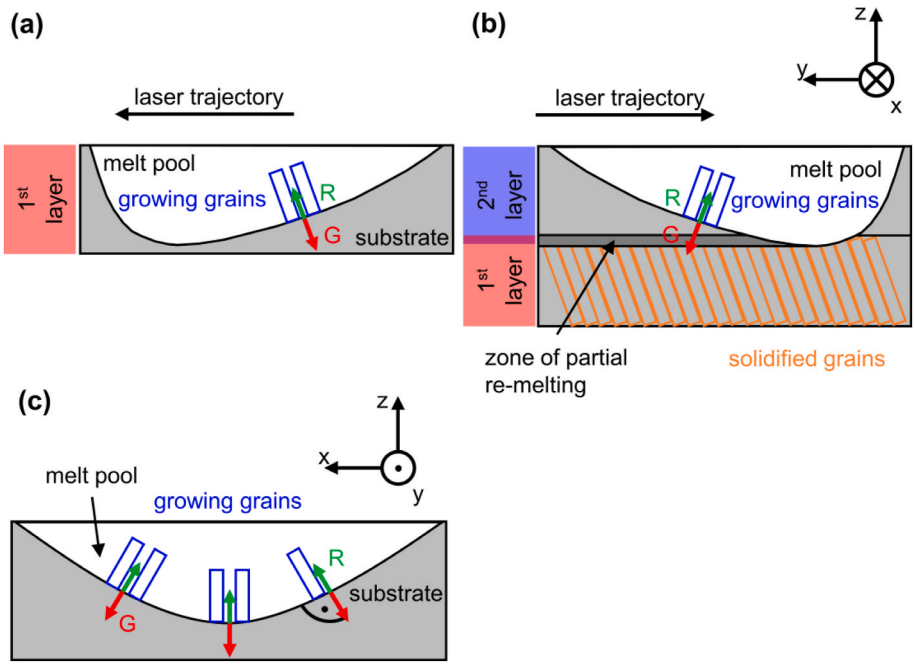

Fig. 4. Schematics visualizing the heat flow and solidification conditions in longitudinal view during DED-LB/M (a) in the first layer and (b) second layer. (c) A visualization in the cross-sectional view. Note that y-direction is equivalent to the laser feed motion direction in the first layer. (a), (c) developed on basis of reports on electron beam powder-bed fusion [43]. See text for details.

Furthermore, these grains exhibit varying growth directions, approximated by inclinations of about +30° to +45° and −30° to −45° with respect to the y-axis. On the contrary, the right side of the xz-IPFM of NHT sample visualizes a region exhibiting a more complex grain growth; grains are seen oriented partially toward BD, accompanied by some equiaxed grains, whereas the center and left show a transition of grains first elongated with an inclination of 45° to the z-axis and, on the left, with 90° angle, respectively. The top IPFM, representing the xy-plane of NHT sample, illustrates grains mostly growing across almost the entire length of the observation area. Furthermore, they are characterized by a comparatively narrow width in x-direction and pronounced length along y-direction, thus resembling the trajectory of the laser deposition in the respective layer. These grains show a preferential <001> orientation with respect to the z-direction. This observation is underlined by the inverse pole figure (IPF) plot shown on the left of Fig. 3 (b), revealing a pronounced <001> texture.

The observed microstructural evolution of the NHT condition can be rationalized by the heat flow conditions prevailing during DED-LB/M, as schematically illustrated in Fig. 4. It is well-established that the microstructural morphology and size of alloys with cubic lattices upon solidification are strongly depended on the temperature gradient G and solidification rate R as well as the incumbent cooling rate β [42].

As a result of the inherent temperature gradients being oriented perpendicular to the melt pool boundary, grains preferentially grow parallel to it, eventually leading to directional solidification [43]. These considerations allow for an explanation of grain growth inclined towards the laser feed motion, as identified in the IPFMs in Fig. 3 (a). Since the laser trajectory is altered by 180° after deposition of each respective layer, the grains growing from the following layer eventually alter their orientation, as dictated by the present heat flow conditions imposed by the melt pool boundaries, while the underlying layer is already solidified with grains elongated to the opposite direction, see Fig. 4 (b). Grain size and morphology observed on the xz-plane of NHT sample as depicted in Fig. 3 (a) may be explained using the corresponding heat flow assumptions in the cross-sectional view shown in Fig. 4 (c), but also taking into account the repetitive partial re-melting of neighboring tracks due to the overlap of approximately 20 % set in present experiments. Obviously, the presented results in terms of grain growth direction are in excellent agreement to previous reports in the field of DED-LB/M [44–46].

In contrast, the aforementioned features are not observed in the HT condition, shown in Fig. 3 (b). Rather, the grains feature varying grain sizes as well as annealing twins, thus yielding alternating grain aspect ratios. Furthermore, no preferential orientation is derivable from the IPFM plotted with respect to BD. Consequently, the IPF plot on the right of Fig. 3 (b) does not indicate a pronounced texture following heat-treatment, which may be resulting from recrystallization. Observations on the weakening and randomization of texture in PBF-LB AISI 316L SS following recrystallization annealing at 1150 °C have recently been published by Pinto et al. [47] and were attributed to the absence of strain when nucleating new grains. In light of the similarities between the employed temperature-regimes during annealing, the aforementioned mechanism readily explains the absence of a pronounced texture in the HT condition seen in the present study.

Furthermore, face-centered cubic (fcc) alloys have proved to exhibit grain growth with preferential <001> orientation along the heat flow direction, i.e., orientation of the temperature gradient [48]. Since there is no surrounding powder bed in DED processes that could provide additional heat conduction, but rather an argon shielding gas atmosphere acting as further insulation, heat flow from top to bottom of the processed structure is exacerbated. As a result, the presented NHT sample exhibits a pronounced <001> texture along the z-direction. The aforementioned fcc crystal structure can be confirmed for both sample conditions throughout, as Fig. 5 (a) visualizes.

It is also notable that no body centered cubic (bcc) ferrite phases have been detected in either of the samples. Moreover, the detailed analysis of grain boundaries in Fig. 5 (b) visualizes that almost 50 % of the grain boundaries in the HT sample are coincident site lattices (CSL) of type Σ3, i.e., twin boundaries. On the contrary, the fraction of Σ3-boundaries in the NHT condition only is around 0.5 %. Furthermore, the grain size varies from an average of 59.0 μm in NHT to 71.4 μm in the HT condition.

The solidification mode of austenitic stainless steels following laser materials processing is known to be depended on both variations of

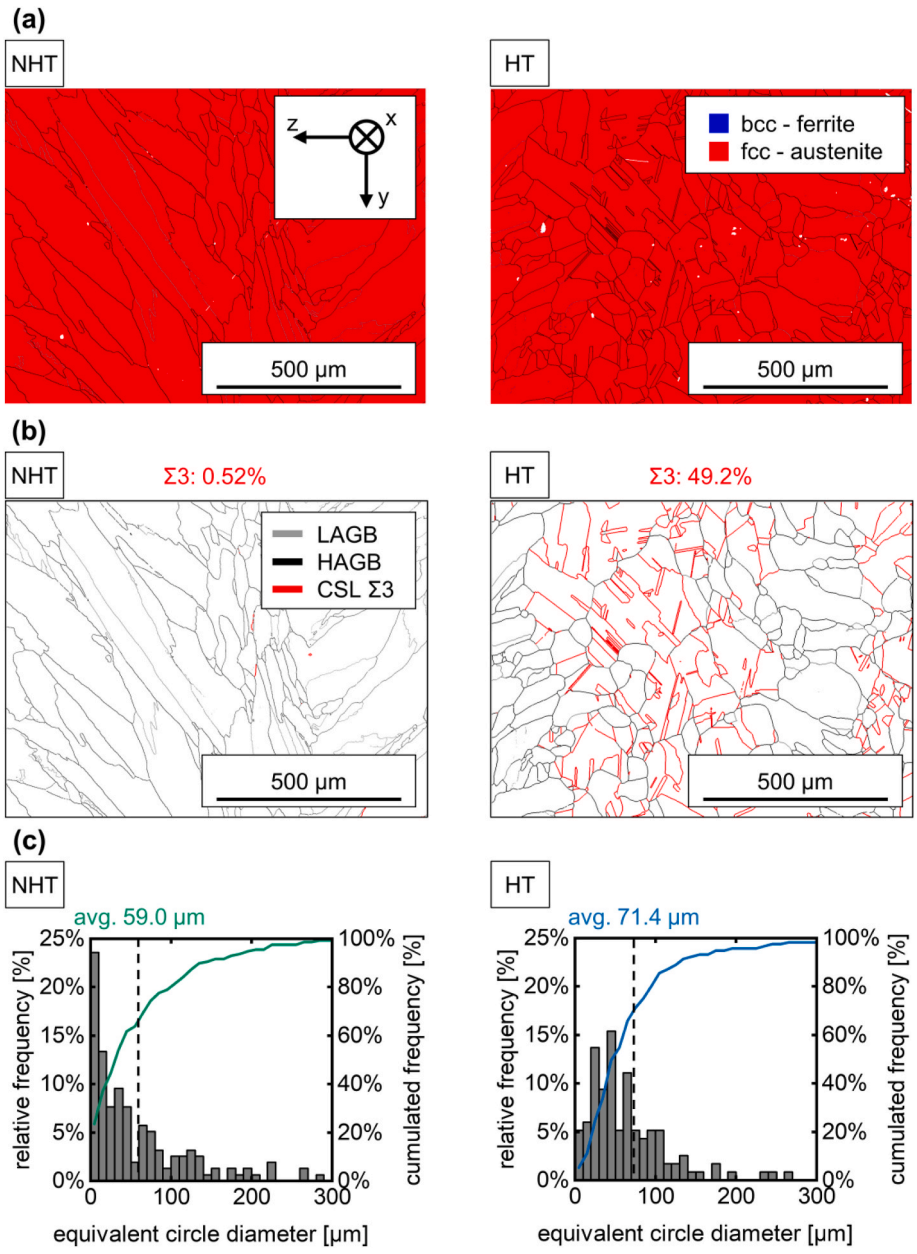

Fig. 5. Phase and grain analysis of the DED-LB/M processed samples along the yz-plane: (a) depicts phase mappings, (b) visualizes the corresponding low-angle grain boundaries (LAGB, 5°–15°, gray), high-angle grain boundaries (HAGB, >15°, black) and CSL Σ3 boundaries (red). (c) shows the calculated grain size evolution as relative and cumulated frequency. Average grain size values are indicated by the dashed line, Σ3 boundaries have been deliberately omitted for grain size analysis.

process parameters [49] as well as composition [50,51]. Considering the chemical composition of the employed grade, which is summarized in Table 1, and utilizing the respective chromium and nickel equivalents presented by Schaeffler [52], the Cr_{eq}/Ni_{eq} ratio is computed to be approximately 1.29. In congruence with another report on DED-LB/M on 316L by Smith et al. [50], the computed ratio pinpoints at a primarily austenitic solidification mode. Consequently, the absence of ferrite in the phase compositions presented in the foregoing text can be rationalized. As with regard to the CSL Σ3 boundaries and grain size differences between the two sample conditions, it shall be noted that the emergence of annealing twins, as indicated by the presence of CSL Σ3 boundaries, in AISI 316L SS resulting from the recrystallization heat treatments is well-documented in literature [53,54]. As it is reported that the grain size and twin fraction increase with prolonged recrystallization duration [54], the larger quantities of CSL Σ3 boundaries in the HT sample in contrast to the NHT condition can be readily explained. Based on these considerations, it is plausible that the NHT sample did not reach a sufficient time-temperature regime during build-up to initiate the formation of annealing twins, hence the comparatively low quantity of CSL Σ3 boundaries is seen.

3.2. Dynamic tensile testing and post-mortem characterization

The stress-strain response of the different sample conditions upon dynamic tensile loading is depicted in Fig. 6 (a). The NHT samples show a strain rate dependent behavior, as it can be inferred from the variations in tensile response.

At a strain rate of 100 s^{-1}, the stress-strain curves are characterized by similar behavior to quasi-static curves (i.e., 0.001 s^{-1} strain rate) of DED-LB/M AISI 316L SS, e.g. Ref. [54], with obvious work hardening following the yield point. At higher strain rates of 500 s^{-1} and 1000 s^{-1}, the specimens are characterized by an increased flow stress (see

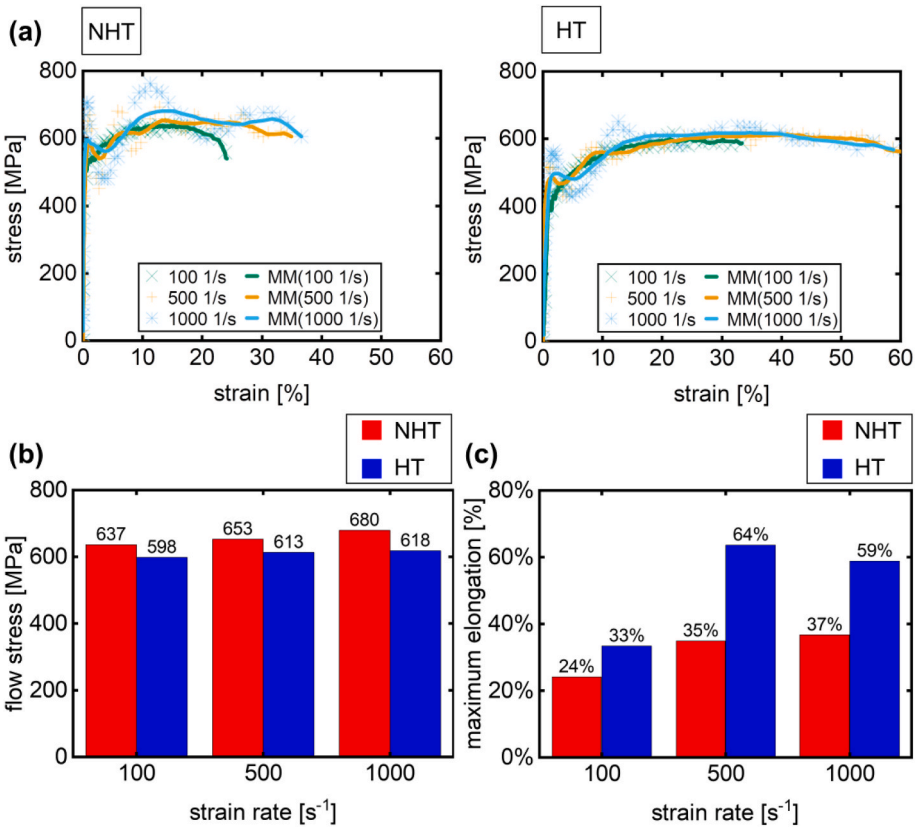

Fig. 6. Results of dynamic tensile testing at various strain rates: (a) depicts the obtained stress-strain curves plotted as MM from the obtained data points. For the sake of readability, only every 10th and 2nd data point is depicted in the plots for strain rates of 100 s^{-1} and 500 s^{-1}, respectively; (b) and (c) show a summary of the derived mechanical properties.

summary of derived properties in Fig. 6 (b)).

The superior yield strength of NHT AISI 316L SS, processed by DED-LB/M, has been documented in literature under compressive and tensile, low-strain rate loading beforehand [30,55,56] and has been attributed to high dislocation density as well as extremely fine microstructural features. It is therefore reasonable to infer that the aforementioned strengthening mechanisms, particularly a higher dislocation density and smaller grain size, are the root cause of the superior yield strength of the NHT specimens.

For all investigated specimens, the flow stress is increased with increasing strain rate. Similar observations have been made by Song et al. [34] during dynamic tensile testing of AISI 304L SS, fabricated by DED-LB/M. As for bulk material, Lee et al. [57] attributed increasing flow stresses of AISI 316L SS during dynamic testing to intragranular slip bands, effectively acting as obstacles to dislocation motion. Furthermore, it was mentioned that these slip bands also increased the interaction of dislocations with adjacent slip bands. Such combined effects lead to higher resistance to dislocation movement at high strain rates and, consequently, strengthening effects. Analog to the NHT specimens, the HT specimens are characterized by work hardening after yielding. Yet, the detected flow stress increase with increasing strain rate is far less pronounced as in case of the NHT specimens. Furthermore, the yield strengths of the HT specimens are well below that of the corresponding NHT specimens, thus further underlining the importance of fine microstructural features and high dislocation density as discussed beforehand. Obviously though, the uncertainty due to the test rig oscillations and the incumbent waviness of the stress-strain curves, particularly present at the transition domain of elastic to plastic material behavior, has to be taken into account and cannot be fully compensated through the use of the MM.

An increase of total elongation to failure is clearly evident with increasing strain rate for the investigated NHT specimens, as is summarized in Fig. 6 (c). Furthermore, a similar behavior in terms of maximum elongation to failure can be perceived for HT specimens with increasing strain rate, although the obtained maximum elongations are almost twice as high as in the NHT specimens.

To shed further light on the underlying deformation mechanisms during dynamic tensile testing, the local strain evolution as obtained by DIC is plotted at varying global strain levels ε_{zz} in Fig. 7. The depicted plots showcase substantial differences in local strain distribution depending on the sample condition. Exemplary, at a strain rate of 100 s^{-1}, the NHT specimen reaches a local strain maximum of approximately 40 % at a global strain level of 20 %, as Fig. 7 (a) reveals. In contrast, the HT specimen only surpasses this local strain maximum at the global strain of 30 %. Consequently, strain localization is to occur at earlier stages in the case of the NHT specimen. These observed differences in local strain maxima and distributions are continued through all investigated strain rates, i.e., strain localization occurs at a later stage for the HT specimens, which is obvious from the comparison of respective DIC images. This leads to the conclusion that necking is initiated at a lower global strain level in the NHT condition as well, which is in excellent agreement to the generally higher failure strains presented in Fig. 6 (a) and the higher elongation to failure depicted in Fig. 6 (c) for the HT condition.

Therefore, it is reasonable to infer that recrystallization annealing significantly affects strain localization and, on basis of that, necking behavior during dynamic tensile testing.

The observed differences in dynamic tensile behavior between NHT and HT specimens are also underlined by the fractography analysis depicted in Fig. 8.

Please note that the samples tested at a strain rate of 1000 s^{-1} were selected for further *post-mortem* investigations on basis of their large

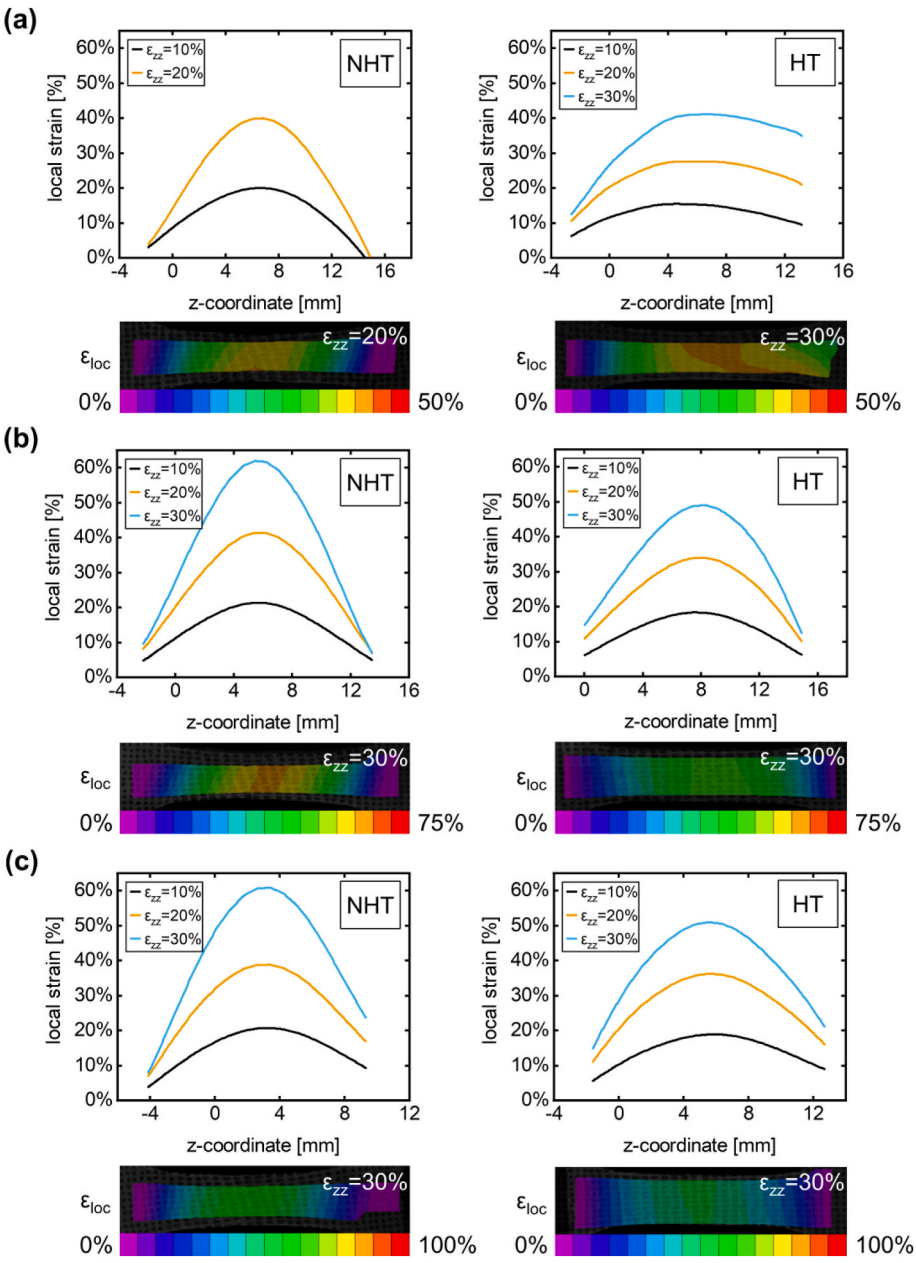

Fig. 7. Local strain evolution during dynamic tensile testing of each condition at different global strain levels ε_{zz} during testing at nominal strain rates of (a) 100 s^{-1}, (b) 500 s^{-1} and (c) 1000 s^{-1}. Bottom images depict corresponding strain distributions obtained by DIC at the maximum global strain level ε_{zz} indicated on the top right of the image. Note that DIC images have been adjusted in aspect ratio to fit the above graphs. Video recordings of all high-speed DIC measurements at 100 s^{-1} and 1000 s^{-1} are available as supplementary material.

differences in flow stress and elongation to failure. Macroscopic images in Fig. 8 (a) reveal a cup-and-cone fracture morphology in the NHT condition at a strain rate of 1000 s^{-1}. On the contrary, the HT specimen is characterized by shear fracture with a fracture surface inclination of 45° with respect to LD. Related differences can be identified on the fracture surface as well, as Fig. 8 (b) visualizes. Evidently, the fracture surface of the NHT specimens exhibits only minimal topography and, thus, may be described by a rather flat appearance. However, a more detailed image of the fracture surface reveals the formation of equiaxed dimples. Consequently, the prevailing failure mechanism of the NHT is ductile, although some river pattern and, thus, localized indications of cleavage fracture are observed as well. A pore with an approximate diameter of less than 25 μm is also seen on the fracture surface. Based on its size, this pore was detected by the automated image binarization routine, whose results are depicted in Fig. 2. Thus, even pores of such size eventually contributed to the calculated porosity levels. Evidently, no crack propagation traces are visible around the pore. Based on this observation and the overall flat appearance of the fracture surface, it is concluded that the depicted pore was torn apart during testing. In congruence with reports by Fadida et al. [28], the pore diameter identified in the specimen at hand can thus be described as non-critical to the failure mechanism during dynamic loading, which is obviously governed by other factors.

On the contrary, the fracture surface of the HT specimen is characterized by a substantially different topography. A magnified image of the fracture surface highlights the formation of dimples in the analog size range to the NHT condition, yielding a ductile failure mechanism for the HT condition as well. Notably, a pore with similar diameter of less than 25 μm can be identified on the fracture surface. This pore contributed to the calculated porosity levels in Fig. 2, taking into account the resolution

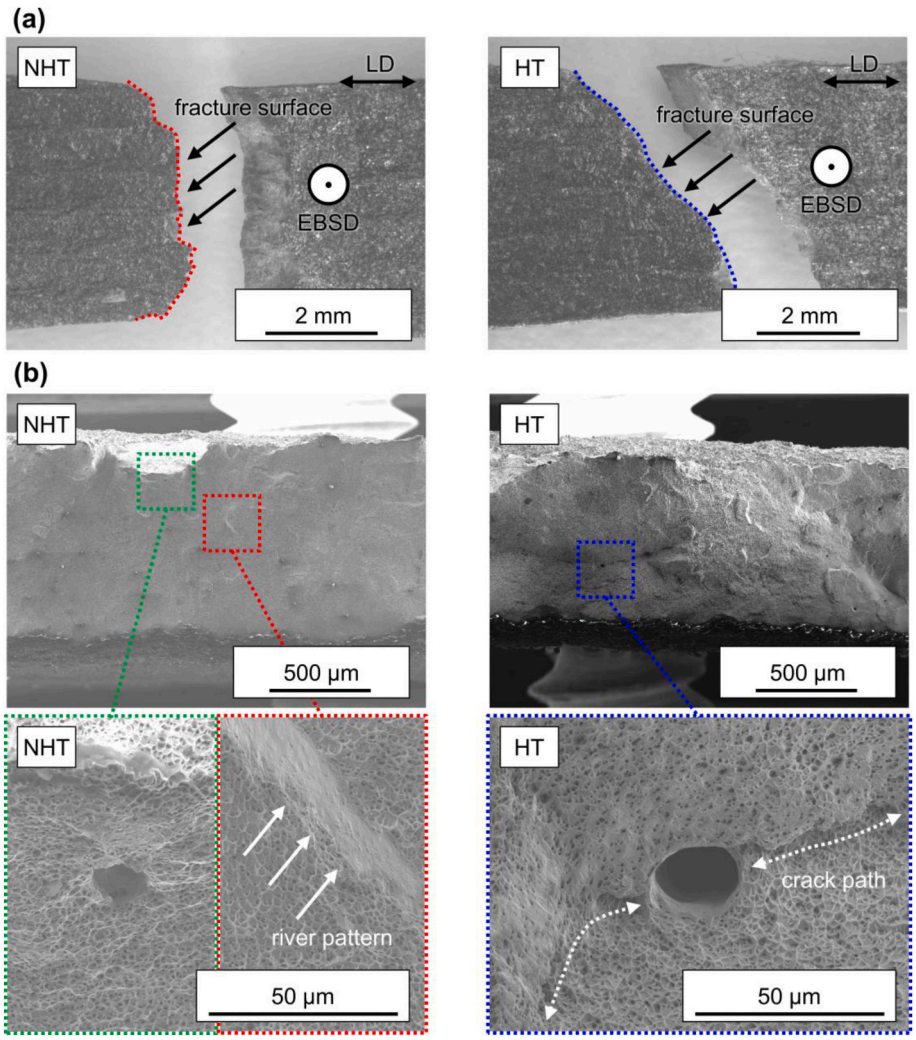

Fig. 8. Fractography analysis of specimens after dynamic tensile testing with a nominal strain rate of 1000 s^{-1} for the NHT (left column) and the HT condition (right column): (a) shows optical micrographs of the fractured specimens, markings represent ROI for subsequent EBSD analysis depicted in Fig. 9; (b) visualizes corresponding secondary electron images of the fracture surfaces.

employed during image binarization. In this case, however, the crack path during failure propagates along the depicted pore. In consideration of the superior failure strain of nearly 60 %, this pore seemingly plays a subordinate role in the failure mechanism of the HT specimen.

As is evidenced by the variations in dynamic tensile response, local strain distribution and fracture morphology, the microstructural features presented and discussed previously must be responsible for the alternating behavior. An EBSD analysis of the deformed microstructure, presented in Fig. 9, sheds light on the underlying mechanisms. The superimposed IPFM and band contrast images shown in Fig. 9 (a) visualize varying grain orientations in a reoccurring zebra-pattern and a substantially deformed microstructure, as is underlined by the poor band contrast in a number of areas. A detailed analysis of grain boundaries in conjunction with the misorientation angle, depicted in Fig. 9 (b) and (c), confirms the formation of CSL Σ3 grain boundaries, indicating deformation twinning, in the deformed microstructure of NHT and HT specimen.

Notably, there appear to be more CSL Σ3 grain boundaries and, thus, twins in the HT than in the NHT condition. As can be derived from direct comparison of the IPFMs plotted above, twinning appears to be most active in grains exhibiting a near <111> orientation along LD and is absent in grains with <001> orientation. Furthermore, the <001> oriented and near-<001> oriented grains feature a high degree of kernel average misorientation (KAM) in both NHT and HT condition. The formation of twins and, in particular, its positive effect on plastic deformation behavior has been already observed in PBF-LB/M AISI 316L SS under quasi-static [58–60] and dynamic compressive loading [61]. Similar to the presented results, Pham et al. [58] reported on the absence of twinning in [100] oriented grains (with respect to LD/BD) as well as strong slip activity therein.

The competing deformation mechanisms of slip and twinning have been found to be orientation-depended phenomena in austenitic stainless steels [62]. While slip is the dominant deformation mechanism in [001] oriented grains (due to the low Schmid-factor in [001] grains of fcc materials [63]), twinning is dominant in [111] oriented grains. Twinning has been observed in [111] oriented single crystals at strains of 3 % and above, while twinning only emerges at 10 % or above in [001] oriented single crystals [62]. In consideration of these reports, the differences in total elongation to failure as well as flow stress in the present investigation can be readily explained. Based on the pronounced <001> texture seen in the NHT samples, a reduced probability for twinning can be anticipated as slip is the dominant deformation mechanism in <001> oriented grains. Consequently, a lower number of CSL Σ3 grain boundaries proved to be detectable through EBSD measurements. As has been already discussed in the preceding section, recrystallization through heat treatment significantly affects texture and, thus, opens pathways for more frequent twinning. It has been reported that annealing twins in AISI 316L SS decay upon deformation, eventually

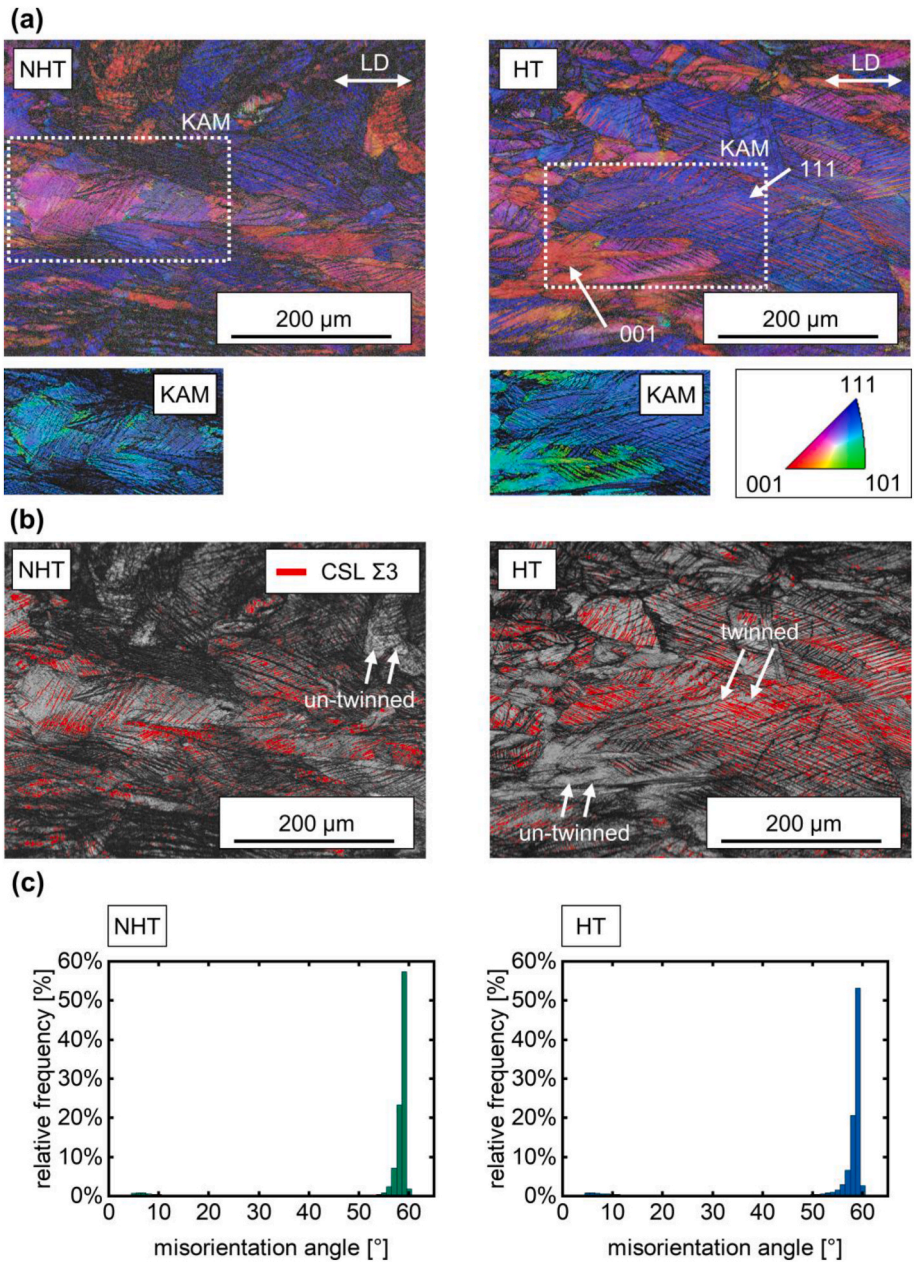

Fig. 9. Post-mortem microstructure analysis after dynamic tensile testing with a nominal strain rate of 1000 s^{-1}. Data were obtained in close vicinity to the fracture surfaces as indicated in Fig. 8; (a) illustrates the superimposed band contrast and inverse pole figure mapping; orientations are plotted for LD, which is equivalent to BD, inset images depict the KAM for regions being located in the dotted rectangles appended above; (b) depicts the corresponding band contrast and CSL Σ3 grain boundaries marked in red; (c) visualizes misorientation angle distribution as derived from EBSD data.

acting as base for generation of deformation twins [64]. The large fraction of CSL Σ3 grain boundaries in the undeformed HT condition can, thus, act as reservoir for twin decay and subsequent emergence of deformation twins upon dynamic tensile loading.

As for the observed differences in flow stress between the NHT and the HT condition, it has been reported for magnesium alloy AZ31 that the activation of multiple slip systems requires differing levels of critical resolved shear stress at varying strain rates [65]. Consequently, the activation of multiple slip systems in the NHT condition may require different stress levels as well. Eventually, this leads to an increase of flow stress with increasing strain rate. Furthermore, the absence of a pronounced increase in flow stress with increasing strain rate in the case of the HT specimens, i.e., where twinning is additionally promoted, underlines this rationale. In addition, twins limit the mean free path for dislocation movement and, thus, reduce the total number of accumulated dislocations at a single given twin boundary [65,66]. Consequently, lower local and more evenly distributed stresses arise, eventually leading to less deformed grains in general [65]. This reduced level of, and more equally distributed, deformation is evidenced by the DIC images presented in Fig. 7; this finding eventually justifies the higher fracture elongations of the HT condition and delayed necking. It needs to be mentioned that grains with <001> orientation in the HT samples still lack twinning in contrast to <111> oriented grains. This rationale is further supported by the high KAM in the <001> oriented grain presented in Fig. 9 (a), which is an indicator for intense slip activity [58].

Moreover, the observed pores in Fig. 8 obviously play a subordinate role with respect to the damage tolerance of the specimens tested at nominal strain rates of 1000 s^{-1}, underlining the observed microstructural differences. Obviously, twinning in the HT specimen enables far

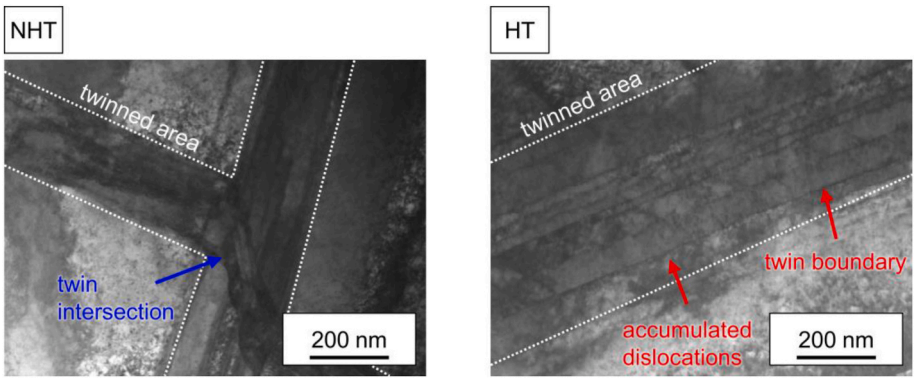

Fig. 10. Bright field STEM images revealing the differences of twin formation in the NHT and the HT condition at a nominal strain rate of 1000 s^{-1}.

higher degrees of plasticity than in the NHT condition. Therefore, the HT specimen can withstand the high dynamic loadings for a prolonged time and, thus, the basis for crack propagation through a wider spatial volume of the sample is provided, as is evidenced by fractography analysis. In contrast, inferior plasticity in the NHT condition leads to shock-response of the material. As a result, it is to be deduced that the plasticity induced by twinning is a decisive factor to obtain a high degree of damage tolerance in the present dynamic tensile loading configuration. A detailed analysis of twin formation in both sample conditions elaborated by STEM is depicted in Fig. 10.

In both sample conditions, twins are characterized by boundaries of dark contrast, which is an indicator for pinned dislocations [67]. Furthermore, the vertically-oriented twins in the NHT condition are intersected by another set of twins originating from the left hand side. Such twin intersections, observed in the NHT condition, do not favor the continuous deformation via twinning. In the HT condition, such interactions are seldomly seen and the twins, arranged parallel to each other, make up for a larger total area fraction. This supports the aforementioned findings with regard to the role of twinning on the plastic deformation behavior and, thus, underlines the provided rationale for excellent ductility of heat treated AISI 316L SS during dynamic tensile loading.

4. Conclusions

The present investigation studied the deformation behavior of AISI 316L SS fabricated by DED-LB/M in non-heat-treated (NHT) as well as heat treated (HT) condition and, thus, provided novel insight on the inherent deformation mechanisms during dynamic tensile loading. From the results presented beforehand, the following conclusions can be drawn.

- Upon fabrication by DED-LB/M, AISI 316L SS was found to be excellently suited for dynamic tensile loading owing to the presence of a ductile failure mechanism in NHT and HT condition.
- The mechanical properties during dynamic tensile loading were strongly dependent on the sample condition. NHT specimens were characterized by higher yield stress and reduced total elongation to failure, while HT specimens exhibited superior ductility with fracture strains of around 60 %.
- Twinning was found to be responsible for the excellent ductility in the HT condition due to the decay of prior annealing twins as well as the emergence of deformation twins. As expected, twinning was absent in <001> oriented grains in both NHT and HT condition, further emphasizing the important role of grain orientation for deformation twinning. Given its randomized grain orientations, the HT condition exhibited more pronounced twinning than the NHT condition.
- The differences in twin formation could be confirmed using EBSD measurements and bright field STEM images, both revealing a larger area fraction of twins in the HT condition.
- As twinning led to a reduction of the mean free path of dislocations, the stresses upon loading and dislocation movement in the HT samples were distributed more evenly, eventually leading to reduced local strains at a given nominal strain value and delayed necking.
- Based on the level of ductility obtained for both conditions, the specimens showed superior resistance against detrimental effects of defects in the form of cylindrical pores, which were observable at the given detection precision following image binarization.

In light of the presented results, further investigations to understand the effects of build orientation with respect to load direction are suggested. Based on scarce literature in the field of dynamic tensile loading of additively manufactured components, it is to be anticipated that the aforementioned combination of *in situ* DIC measurements and high strain rate deformation may provide insights into the deformation characteristics of a multitude of other alloys, specifically those important for AM.

CRediT authorship contribution statement

N. Sommer: Conceptualization, Data curation, Formal analysis, Funding acquisition, Investigation, Methodology, Project administration, Validation, Visualization, Writing – original draft, Writing – review & editing. **S. Lee:** Data curation, Formal analysis, Investigation, Writing – review & editing. **F. Stredak:** Formal analysis, Investigation. **C. Wolf:** Formal analysis, Investigation, Data curation. **A. Suckau:** Formal analysis, Investigation, Data curation. **M. Vollmer:** Formal analysis, Investigation, Writing – review & editing. **S. Shao:** Funding acquisition, Formal analysis, Investigation, Validation, Resources, Writing – review & editing. **T. Niendorf:** Funding acquisition, Supervision, Validation, Writing – review & editing. **N. Shamsaei:** Funding acquisition, Formal analysis, Supervision, Validation, Resources, Writing – review & editing. **S. Böhm:** Funding acquisition, Supervision, Validation, Writing – review & editing.

Declaration of competing interest

The authors declare that they have no known competing financial interests or personal relationships that could have appeared to influence the work reported in this paper.

Acknowledgements

Niklas Sommer acknowledges funding within the framework of a postdoc stipend provided by the Department for Internationalization and International Cooperation of the University of Kassel. Thomas

Niendorf acknowledges funding by Deutsche Forschungsgemeinschaft (Project ID: 433662460). S. Lee, S. Shao, and N. Shamsaei acknowledge partial support from the United States National Aeronautics and Space Administration (NASA) under Award No. 80NSSC21M0361.

Appendix A. Supplementary data

Supplementary data to this article can be found online at https://doi.org/10.1016/j.jmrt.2023.10.251.

References

[1] Gibson I, Rosen D, Stucker B, Khorasani M. Additive manufacturing technologies. Cham: Springer International Publishing; 2021.
[2] Zhang Guo X, Kane, S, Deng Y, Jung Y-G Y, Wu L, et al. Additive manufacturing of metallic materials: a review. J Mater Eng Perform 2018;27(1):1–13. https://doi.org/10.1007/s11665-017-2747-y.
[3] Deutsches Institut für Normung e. V. Additive manufacturing - general principles - terminology (ISO/ASTM DIS 52900:2018), German and English version prEN ISO/ASTM 52900:2018, DIN EN ISO/ASTM 52900; Beuth Verlag GmbH: Berlin, Germany, 2018.
[4] Sommer N., Kluge P., Stredak F., Eigler S., Hill H., Niendorf T., et al. Additive manufacturing of compositionally-graded AISI 316L to CoCrMo structures by directed energy deposition. Crystals 2021;11(9):1043. https://doi.org/10.3390/cryst11091043.
[5] Groden C, Champagne V, Bose S, Bandyopadhyay A. Inconel 718-CoCrMo bimetallic structures through directed energy deposition-based additive manufacturing. Mater Sci Add Manuf 2022;1(3):18. https://doi.org/10.18063/msam.v1i3.18.
[6] Sommer N, Bauer A, Kahlmeyer M, Wegener T, Degener S. Liehr A., et al. High-throughput alloy development using advanced characterization techniques during directed energy deposition additive manufacturing. Adv Eng Mater 2023:2300030. https://doi.org/10.1002/adem.202300030.
[7] Shamsaei N, Yadollahi A, Bian L, Thompson SM. An overview of Direct Laser Deposition for additive manufacturing; Part II: mechanical behavior, process parameter optimization and control. Addit Manuf 2015;8:12–35. https://doi.org/10.1016/j.addma.2015.07.002.
[8] Zhou H, Yang Y, Han C, Wei Y, Liu Z, Tai Z, et al. Laser directed energy deposition/milling hybrid additive manufacturing of thin-walled GH4169 alloy: effect of processing strategy on its microstructure and mechanical properties. Mater Sci Eng 2023;882:145480. https://doi.org/10.1016/j.msea.2023.145480.
[9] Niendorf T, Leuders S, Riemer A, Richard HA, Tröster T, Schwarze D. Highly anisotropic steel processed by selective laser melting. Metall Mater Trans B 2013;44(4):794–6. https://doi.org/10.1007/s11663-013-9875-z.
[10] Aversa A, Marchese G, Bassini E. Directed energy deposition of AISI 316L stainless steel powder: effect of process parameters. Metals 2021;11(6):932. https://doi.org/10.3390/met11060932.
[11] Margerit P, Weisz-Patrault D, Ravi-Chandar K, Constantinescu A. Tensile and ductile fracture properties of as-printed 316L stainless steel thin walls obtained by directed energy deposition. Addit Manuf 2021;37:101664. https://doi.org/10.1016/j.addma.2020.101664.
[12] Yadollahi A, Shamsaei N. Additive manufacturing of fatigue resistant materials: challenges and opportunities. Int J Fatig 2017;98:14–31. https://doi.org/10.1016/j.ijfatigue.2017.01.001.
[13] Muhammad M, Nezhadfar PD, Thompson S, Saharan A, Phan N, Shamsaei N. A comparative investigation on the microstructure and mechanical properties of additively manufactured aluminum alloys. Int J Fatig 2021;146:106165. https://doi.org/10.1016/j.ijfatigue.2021.106165.
[14] Pegues JW, Roach MD, Shamsaei N. Additive manufacturing of fatigue resistant austenitic stainless steels by understanding process-structure–property relationships. Materials Research Letters 2020;8(1):8–15. https://doi.org/10.1080/21663831.2019.1678202.
[15] Cheruvathur S, Lass EA, Campbell CE. Additive manufacturing of 17-4 PH stainless steel: post-processing heat treatment to achieve uniform reproducible microstructure. JOM 2016;68(3):930–42. https://doi.org/10.1007/s11837-015-1754-4.
[16] Kanagarajah P, Brenne F, Niendorf T, Maier HJ. Inconel 939 processed by selective laser melting: effect of microstructure and temperature on the mechanical properties under static and cyclic loading. Mater Sci Eng 2013;588:188–95. https://doi.org/10.1016/j.msea.2013.09.025.
[17] Brenne F, Taube A, Pröbstle M, Neumeier S, Schwarze D, Schaper M, et al. Microstructural design of Ni-base alloys for high-temperature applications: impact of heat treatment on microstructure and mechanical properties after selective laser melting. Prog Addit Manuf 2016;1(3–4):141–51. https://doi.org/10.1007/s40964-016-0013-8.
[18] Moran TP, Carrion PE, Lee S, Shamsaei N, Phan N, Warner DH. Hot isostatic pressing for fatigue critical additively manufactured Ti-6Al-4V. Materials 2022;15(6):2051. https://doi.org/10.3390/ma15062051.
[19] Nezhadfar PD, Burford E, Anderson-Wedge K, Zhang B, Daniewiz S, Shao SR, et al. Fatigue crack growth behavior of additively manufactured 17-4 PH stainless steel: effects of build orientation and microstructure. Int J Fatig 2019;123:168–79. https://doi.org/10.1016/j.ijfatigue.2019.02.015.
[20] Ramesh KT. High rates and impact experiments. In: *Springer Handbook of experimental solid mechanics* (springer handbooks), W. N. Sharpe. Boston, MA: Springer US; 2008. p. 929–60.
[21] Alkhatib SE, Sercombe TB. High strain-rate response of additively manufactured light metal alloys. Mater Des 2022;217:110664. https://doi.org/10.1016/j.matdes.2022.110664.
[22] Hadadzadeh A, Amirkhiz BS, Odeshi A, Mohammadi M. Dynamic loading of direct metal laser sintered AlSi10Mg alloy: strengthening behavior in different building directions. Mater Des 2018;159:201–11. https://doi.org/10.1016/j.matdes.2018.08.045.
[23] Hadadzadeh A, Shalchi Amirkhiz B, Odeshi A, Li J, Mohammadi M. Role of hierarchical microstructure of additively manufactured AlSi10Mg on dynamic loading behavior. Addit Manuf 2019;28:1–13. https://doi.org/10.1016/j.addma.2019.04.012.
[24] Baxter C, Cyr E, Odeshi A, Mohammadi M. Constitutive models for the dynamic behaviour of direct metal laser sintered AlSi10Mg_200C under high strain rate shock loading. Mater Sci Eng 2018;731:296–308. https://doi.org/10.1016/j.msea.2018.06.040.
[25] Isaac JP, Lee S, Thompson S, Saharan A, Shamsaei N, Tippur HV. Role of build orientation on quasi-static and dynamic fracture responses of additively manufactured Alf357 and Alsi10mg alloys. SSRN Journal 2022. https://doi.org/10.2139/ssrn.4115539.
[26] Maconachie Leary M, Zhang J, Medvedev A, Sarker A, Ruan D T, et al. Effect of build orientation on the quasi-static and dynamic response of SLM AlSi10Mg. Mater Sci Eng 2020;788:139445. https://doi.org/10.1016/j.msea.2020.139445.
[27] Jakkula P, Ganzenmüller G, Gutmann F, Pfaff A, Mermagen J, Hiermaier S. Strain rate sensitivity of the additive manufacturing material scalmalloy. J. dynamic behavior mater. 2021;7(4):518–25. https://doi.org/10.1007/s40870-021-00298-4.
[28] Fadida R, Shirizly A, Rittel D. Dynamic tensile response of additively manufactured Ti6Al4V with embedded spherical pores. J Appl Mech 2018;85(4):41004. https://doi.org/10.1115/1.4039048.
[29] Du K, Yang L, Xu C, Wang B, Gao Y. High strain rate yielding of additive manufacturing Inconel 625 by selective laser melting. Materials 2021;14(18):5408. https://doi.org/10.3390/ma14185408.
[30] Gray G.T., Livescu V., Rigg P.A., Trujillo C.P., Cady C.M., Chen S.R., et al. Structure/property (constitutive and dynamic strength/damage) characterization of additively manufactured 316L SS. EPJ Web Conf 2015;94:2006. https://doi.org/10.1051/epjconf/20159402006.
[31] Gray Livescu V, Rigg PA, Trujillo CP, Cady CM, Chen SR GT, et al. Structure/property (constitutive and spallation response) of additively manufactured 316L stainless steel. Acta Mater 2017;138:140–9. https://doi.org/10.1016/j.actamat.2017.07.045.
[32] Chen Wei H, Bao K, Zhang X, Cao Y, Peng Y J, et al. Dynamic mechanical properties of 316L stainless steel fabricated by an additive manufacturing process. J Mater Res Technol 2021;11(2):170–9. https://doi.org/10.1016/j.jmrt.2020.12.097.
[33] Nishida Song B, Maguire M, Adams D, Carroll J, Wise J E, et al. Dynamic compressive response of wrought and additive manufactured 304L stainless steels. EPJ Web Conf 2015;94:1001. https://doi.org/10.1051/epjconf/20159401001.
[34] Song Nishida E, Sanborn B, Maguire M, Adams D, Carroll J B, et al. Compressive and tensile stress–strain responses of additively manufactured (AM) 304L stainless steel at high strain rates. J. dynamic behavior mater. 2017;3(3):412–25. https://doi.org/10.1007/s40870-017-0122-6.
[35] Scharifi Sajadifar SV, Moeini G, Weidig U, Böhm S, Niendorf T E, et al. Dynamic tensile deformation of high strength aluminum alloys processed following novel thermomechanical treatment strategies. Adv Eng Mater 2020;22(8):2000193. https://doi.org/10.1002/adem.202000193.
[36] Riemer A, Leuders S, Thöne M, Richard HA, Tröster T, Niendorf T. On the fatigue crack growth behavior in 316L stainless steel manufactured by selective laser melting. Eng Fract Mech 2014;120:15–25. https://doi.org/10.1016/j.engfracmech.2014.03.008.
[37] Andreau O, Pessard E, Koutiri I, Peyre P, Saintier N. Influence of the position and size of various deterministic defects on the high cycle fatigue resistance of a 316L steel manufactured by laser powder bed fusion. Int J Fatig 2021;143:105930. https://doi.org/10.1016/j.ijfatigue.2020.105930.
[38] Dass A, Moridi A. State of the art in directed energy deposition: from additive manufacturing to materials design. Coatings 2019;9(7):418. https://doi.org/10.3390/coatings9070418.
[39] Suder WJ, Williams SW. Investigation of the effects of basic laser material interaction parameters in laser welding. J Laser Appl 2012;24(3):032009. https://doi.org/10.2351/1.4728136. Art. no.
[40] Bliedtner J, Müller H, Barz A. Wechselwirkungsprozesse. In: Bliedtner J, Lasermaterialbearbeitung HMüller, Barz A, editors. München. Carl Hanser Verlag GmbH & Co. KG; 2013. p. 110–39.
[41] Ng GKL, Jarfors AEW, Bi G, Zheng HY. Porosity formation and gas bubble retention in laser metal deposition. Appl Phys 2009;97(3):641–9. https://doi.org/10.1007/s00339-009-5266-3.
[42] Kou S. Welding metallurgy. second ed. Hoboken, NJ: Wiley-Interscience; 2003.
[43] Helmer HE, Körner C, Singer RF. Additive manufacturing of nickel-based superalloy Inconel 718 by selective electron beam melting: processing window and microstructure. J Mater Res 2014;29(17):1987–96. https://doi.org/10.1557/jmr.2014.192.
[44] Segerstark A., Andersson J., Svensson L.-E.. Investigation of laser metal deposited Alloy 718 onto an EN 1.4401 stainless steel substrate. Opt Laser Technol 2017;97:144–53. https://doi.org/10.1016/j.optlastec.2017.05.038.

[45] Sreekanth S, Ghassemali E, Hurtig K, Joshi S, Andersson J. Effect of direct energy deposition process parameters on single-track deposits of alloy 718. Metals 2020; 10(1):96. https://doi.org/10.3390/met10010096.
[46] Kiran A, Koukolíková M, Vavřík J, Urbánek M, Džugan J. Base plate preheating effect on microstructure of 316L stainless steel single track deposition by directed energy deposition. Materials 2021;14(18):5129. https://doi.org/10.3390/ma14185129.
[47] Pinto FC, Aota LS, Souza Filho IR, Raabe D, Sandim HRZ. Recrystallization in non-conventional microstructures of 316L stainless steel produced via laser powder-bed fusion: effect of particle coarsening kinetics. J Mater Sci 2022;57(21):9576–98. https://doi.org/10.1007/s10853-021-06859-1.
[48] Thijs L, Kempen K, Kruth J-P, van Humbeeck J. Fine-structured aluminium products with controllable texture by selective laser melting of pre-alloyed AlSi10Mg powder. Acta Mater 2013;61(5):1809–19. https://doi.org/10.1016/j.actamat.2012.11.052.
[49] Pekkarinen J, Kujanpää V. Laser welding parameters effects on austenitic stainless steels welds microstructure. In: International congress on applications of lasers & electro-optics. California, USA: Anaheim; 2010. p. 676–82. https://doi.org/10.2351/1.5062098.
[50] Smith T.R., Sugar J.D., San Marchi C., Schoenung J.M. Microstructural development in DED stainless steels: applying welding models to elucidate the impact of processing and alloy composition. J Mater Sci 2021;56:762–780. doi: 10.1007/s10853-020-05232-y.
[51] Richter J, Bartzsch G, Scherbring S, Bolender A, Vollmer M, Mola J, et al. Metastable CrMnNi steels processed by laser powder bed fusion: experimental assessment of elementary mechanisms contributing to microstructure, properties and residual stress. Sci Rep 2022;12(1):21862. https://doi.org/10.1038/s41598-022-26052-x.
[52] Schaeffler AL. Constitution diagram for strainless steel weld metal. Metal Progress 1949;56(11). 680-680B.
[53] Varin RA, Kruszynska J. Control of annealing twins in type 316 austenitic stainless steel. Acta Metall 1987;35(7):1767–74. https://doi.org/10.1016/0001-6160(87)90122-2.
[54] Lee S, Ghiaasiaan R, Shao S, Gradl PR, Shamsaei N. Additively manufactured 316L stainless steel: effect of heat treatment on microstructure and tensile properties. In: Proceedings of the 33rd annual international solid freeform fabrication symposium – an additive manufacturing conference; 2022.
[55] Yang Yee J, Zheng B, Gasier K, Reynolds T, Clemon L N, et al. Process-structure-property relationships for 316L stainless steel fabricated by additive manufacturing and its implication for component engineering. J Therm Spray Technol 2017;26(4): 610–26. https://doi.org/10.1007/s11666-016-0480-y.
[56] Barkia B Aubry P, Haghi-Ashtiani P, Auger T, Gosmain L, Schuster F, et al. On the origin of the high tensile strength and ductility of additively manufactured 316L stainless steel: multiscale investigation. J Mater Sci Technol 2020;41:209–18. https://doi.org/10.1016/j.jmst.2019.09.017.
[57] Lee W-S, Chen T-H, Lin C-F, Luo W-Z. Dynamic mechanical response of biomedical 316L stainless steel as function of strain rate and temperature. Bioinorgan Chem Appl 2011;2011:173782. https://doi.org/10.1155/2011/173782.
[58] Pham MS, Dovgyy B, Hooper PA. Twinning induced plasticity in austenitic stainless steel 316L made by additive manufacturing. Mater Sci Eng 2017;704:102–11. https://doi.org/10.1016/j.msea.2017.07.082.
[59] Yin YJ, Sun JQ, Guo J, Kan XF, Yang DC. Mechanism of high yield strength and yield ratio of 316 L stainless steel by additive manufacturing. Mater Sci Eng 2019; 744:773–7. https://doi.org/10.1016/j.msea.2018.12.092.
[60] Yang D., Zhao Y., Kan X., Chu X., Sun H., Zhao Z,, et al. Twinning behavior in deformation of SLM 316L stainless steel. Mater Res Express 2022;9(9):96502. https://doi.org/10.1088/2053-1591/ac8bc7.
[61] Güden M, Enser S, Bayhan M, Taşdemirci A, Yavaş H. The strain rate sensitive flow stresses and constitutive equations of a selective-laser-melt and an annealed-rolled 316L stainless steel: a comparative study. Mater Sci Eng 2022;838:142743. https://doi.org/10.1016/j.msea.2022.142743.
[62] Karaman I, Sehitoglu H, Maier H, Chumlyakov Y. Competing mechanisms and modeling of deformation in austenitic stainless steel single crystals with and without nitrogen. Acta Mater 2001;49(19):3919–33. https://doi.org/10.1016/S1359-6454(01)00296-8.
[63] Karaman I, Sehitoglu H, Chumlyakov Y, Maier H, Kireeva I. Extrinsic stacking faults and twinning in hadfield manganese steel single crystals. Scripta Mater 2001; 44(2):337–43. https://doi.org/10.1016/S1359-6462(00)00600-X.
[64] Mishra S, Narasimhan K, Samajdar I. Deformation twinning in AISI 316L austenitic stainless steel: role of strain and strain path. Mater Sci Technol 2007;23(9): 1118–26. https://doi.org/10.1179/174328407X213242.
[65] Berge F, Krüger L, Ouaziz H, Ullrich C. Influence of temperature and strain rate on flow stress behavior of twin-roll cast, rolled and heat-treated AZ31 magnesium alloys. Trans Nonferrous Metals Soc China 2015;25(1):1–13. https://doi.org/10.1016/S1003-6326(15)63572-5.
[66] Christian JW, Mahajan S. Deformation twinning. Prog Mater Sci 1995;39(1–2): 1–157. https://doi.org/10.1016/0079-6425(94)00007-7.
[67] Ghiaasiaan R, Muhammad M, Gradl PR, Shao S, Shamsaei N. Superior tensile properties of Hastelloy X enabled by additive manufacturing. Materials Research Letters 2021;9(7):308–14. https://doi.org/10.1080/21663831.2021.1911870.